RESEARCH ARTICLE | DECEMBER 01 2016

Self-assembled dual-sided hemispherical nano-dimple-structured broadband antireflection coatings

Cheng-Yen Lin; Kun-Yi Lin; Hui-Ping Tsai; ... et. al

Appl. Phys. Lett. 109, 221601 (2016)
https://doi.org/10.1063/1.4971264

Self-assembled dual-sided hemispherical nano-dimple-structured broadband antireflection coatings

Cheng-Yen Lin,[1] Kun-Yi Lin,[2] Hui-Ping Tsai,[3] Yi-Xuan He,[1] and Hongta Yang[1,a)]
[1]*Department of Chemical Engineering, National Chung Hsing University, 145 Xingda Road, Taichung City 40227, Taiwan*
[2]*Department of Environmental Engineering, National Chung Hsing University, 145 Xingda Road, Taichung City 40227, Taiwan*
[3]*Department of Civil Engineering, National Chung Hsing University, 145 Xingda Road, Taichung City 40227, Taiwan*

(Received 16 October 2016; accepted 18 November 2016; published online 1 December 2016)

A non-lithography-based approach is developed in this study for assembling monolayer close-packed hemispherical nano-dimple arrays on both sides of a PET film by a scalable Langmuir-Blodgett technology. The resulting gratings greatly suppress specular reflection and therefore enhance specular transmission for a broad range of visible wavelengths, resulting from a gradual change in the effective refractive index at air/PET interface. The experimental results reveal that the antireflection properties of the as-fabricated coatings are affected by the size of the nano-dimples. Moreover, both optical performances of single-sided and dual-sided nano-dimple-structured coatings have been investigated in this study. *Published by AIP Publishing.*
[http://dx.doi.org/10.1063/1.4971264]

Natural nanostructures, with unique functionalities, have provided a vast range of inspirations for practical applications.[1–4] For example, cicada wings are highly transparent and exhibit less than 1% reflectance over the visible spectrum, owing to the presence of hexagonal arrays of sub-200 nm conical structures on their wings.[5,6] The cone arrays with a period smaller than the propagating wavelength leads to a gradient index of refraction across the interface between air and wing, substantially suppressing Fresnel's reflection.[7,8] Biomimicry of the cicada wing design onto material surfaces is extensively used as an antireflection coating in optical and optoelectronic applications, including displays, solar cell systems, and vehicle dashboards.[9,10]

Comparing to traditional quarter-wavelength antireflection coatings, multilayer antireflection coatings, as well as porous antireflection coatings, biomimetic subwavelength conical-structured coatings give rise to a gradual change in refractive index rather than a sudden one, and display great broadband antireflection properties over a wide range of angles of incidence.[11–13] However, the coatings are often composed of fragile high-aspect-ratio surface geometries and the fabrication procedures usually require complex preparation schemes.[14] Moreover, current top-down lithographic technologies (e.g., photolithography, nanoimprint lithography, and laser interface lithography) for fabricating cicada-wing antireflection coatings are expensive and exhibit limited control over pattern spatial homogeneity and reproducibility.[15–17] In contrast, self-assembled colloidal crystals have been used as etching masks during a reactive ion etching process to template nanostructure arrays, offering a less expensive and simpler methodology in fabricating cicada-wing gratings.[18–21] Unfortunately, bottom-up self-assembly technologies are mostly used in laboratory-scale and it is challenging to scale up these processes.[22–24] Recently, plasmonic antireflection coatings consisting of a subwavelength metal array and a dielectric cover layer by combination of lithography and metal deposition are designed and fabricating, showing a broadband reduction of reflection.[25–28] However, the reactive ion etching process is relatively expensive and highly labor-intensive, and also requires clean room conditions.[29,30]

In this research, we developed a Langmuir-Blodgett-like approach to assemble large-area nano-dimple-structured antireflection coatings in a roll-to-roll compatible manner. Monodispersed silica spheres with diameters of 155 nm and 70 nm were synthesized by the Stöber method.[31] The synthesized Stöber silica spheres were purified in absolute ethanol by repeated centrifugation/re-dispersion cycles to remove impurities, following by re-dispersing in non-volatile ethoxylated trimethylolpropane triacrylate (ETPTA) monomers with 1 vol. % Darocur 1173 as photoinitiator. The silica particle volume fraction was controlled to be 22.5 vol. %. Figure 1 presents a schematic illustration of the fabrication procedure for creating dual-sided hemispherical nano-dimple-structured antireflection coatings. The as-prepared silica/ETPTA suspension was added dropwise, while the ETPTA monomer-covered silica spheres spread rapidly and formed two-dimensional colloidal monolayers at the deionized water surface. A poly(ethylene terephthalate) (PET) film pre-immersed in deionized water was vertically withdrawn at a rate of ~5 cm/min by using a double-sided tape attached to a syringe pump. The floating ETPTA monomer-covered silica colloidal monolayers were uniformly transferred onto both sides of the PET substrate. The capillary action enables the ETPTA monomers to flow and fill the empty space between the silica colloidal crystals and the PET substrate. The sample was then transferred to a pulsed UV curing system to photo-polymerize ETPTA monomers under UV radiation. The silica spheres partially embedded in ETPTA polymeric matrices were finally removed by wet etching in a 2 vol. % hydrofluoric acid aqueous solution to pattern periodic nano-dimple structures.

a)Author to whom correspondence should be addressed. Electronic mail: hyang@dragon.nchu.edu.tw

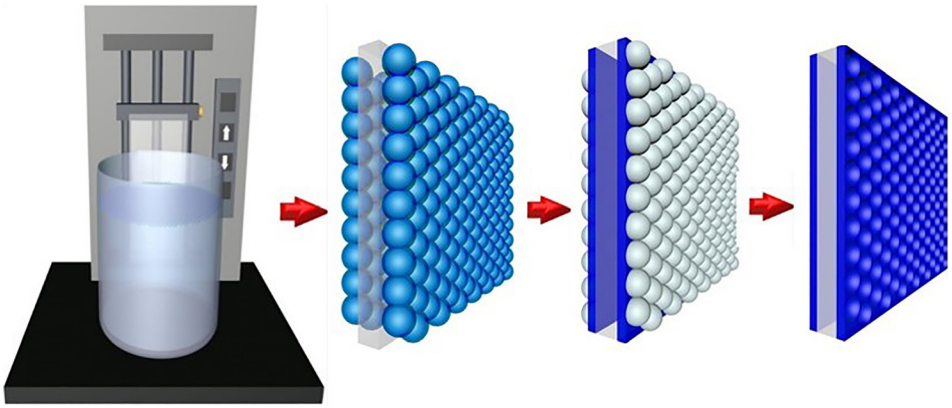

FIG. 1. Schematic illustration of the fabrication procedure for creating dual-sided hemispherical nano-dimple-structured antireflection coatings.

To investigate optical performances of single-sided nano-dimple-structured coatings, the assembled colloidal crystals on one side of the PET film were erased before the photo-polymerization procedure. The top-view SEM image of the PET substrate with single-sided coating in Figure 2(a) illustrates that the hexagonally ordered monolayer 155 nm silica colloidal crystals can be achieved by the self-assembling approach. After removal of the embedded silica spheres, highly ordered nano-dimple arrays are found as shown in Figure 2(b), revealing that the polymeric nano-dimple structures do not collapse during the HF-etching procedure. By averaging the sizes of 100 voids, the void size is estimated as 152 ± 1 nm, which is very close to the diameter of templating silica spheres. This further confirms that the nano-dimples are assembled into a close-packed arrangement. By contrast, even though some defects, including point vacancies and misaligned lines, are presented in the SEM image of the assembled 70 nm silica colloidal crystals, the hexagonal ordered of silica spheres is evidently depicted (Figure 2(c)). The major driving force for the spontaneous crystallization of the colloidal monomers is the capillary action between the neighboring silica spheres at the air/water interface. Since the capillary action is proportional to the size of the colloidal spheres, the crystalline domain size of the 70 nm colloidal coating is smaller than that of the 155 nm colloidal coating.[32] After wet etching, each nano-dimple

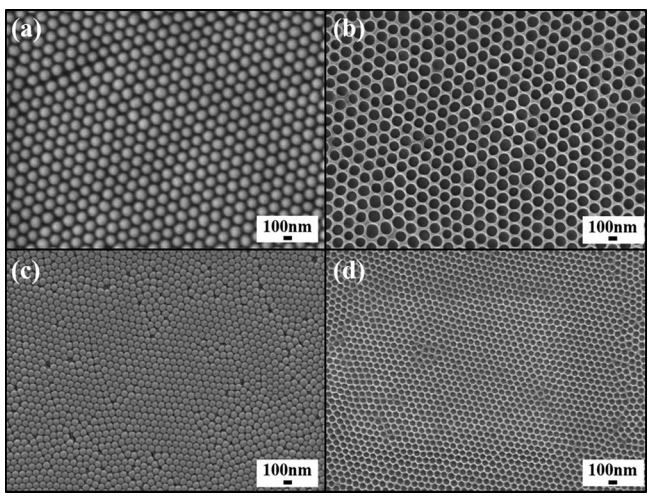

FIG. 2. Top-view SEM images of close-packed colloidal monolayers and the corresponding nano-dimple arrays using silica particles with different sizes. (a) and (b) 155 nm, and (c) and (d) 70 nm.

with an average void size of around 70 nm surrounded by six others can be observed in Figure 2(d), indicating that the coating is composed of hexagonal ordered nano-dimple arrays.

The specular optical reflection and transmission measurements of the self-assembled single-sided hemispherical nano-dimple-structured coatings were evaluated using an UV-visible-near-IR spectrometer (Ocean Optics). Figure 3(a) compares the normal incidence reflection spectra obtained from a flat PET substrate and PET substrates coated with hemispherical 155 nm and 70 nm nano-dimple arrays as displayed in Figure 2. The featureless PET substrate displays a reflectivity of around 8%, resulting from the Fresnel reflection occurs at the air/PET interface. By contrast, the as-fabricated nano-dimple-structured coatings display less than 3% reflectivities for a broad range of visible wavelengths, indicating the great broadband antireflection properties can be achieved. Besides, normal incidence transmission spectra as shown in Figure 3(b) were collected by using the same spectrometer. The 70 nm nano-dimple coating consistently presents higher transmittance (~95%) for the range of visible wavelengths than that of 155 nm nano-dimple coating (~94%), while the bare PET substrate displays lower transmittance (~90%) than those of nano-dimple coatings.

When visible light rays interacting with periodic structures, part of the rays are reflected at the structure surface, and part of that are refracted and therefore lost by absorption within the structures or emerge after several internal reflections. As the coated structure size is less than the visible light wavelength, the propagation of incident light is governed by the change of effective refractive index from air to the substrate. The antireflection properties of the resulting structures can be explained by mapping the calculated effective refractive index across the height of hemispherical nano-dimples (Figure 3(c)). A hemispherical dimple-shaped profile is used to simulate the templated structures as shown in Figures 2(b) and 2(d). Theoretically, the void size equals to the height of nano-dimple structure. The whole structures are divided into 20 layers, and refractive index of each layer can be evaluated from effective medium theory.[8] For the flat PET substrate, the refractive index is greatly increased from 1.0 to 1.58 across the air/PET interface. The discontinuity of the refractive index between air and PET substrate results in higher reflectance. By contrast, the effective refractive index of hemispherical 70 nm nano-dimples is gradually changed from 1.0 to ~1.47 (filled circle), and then sharply increased

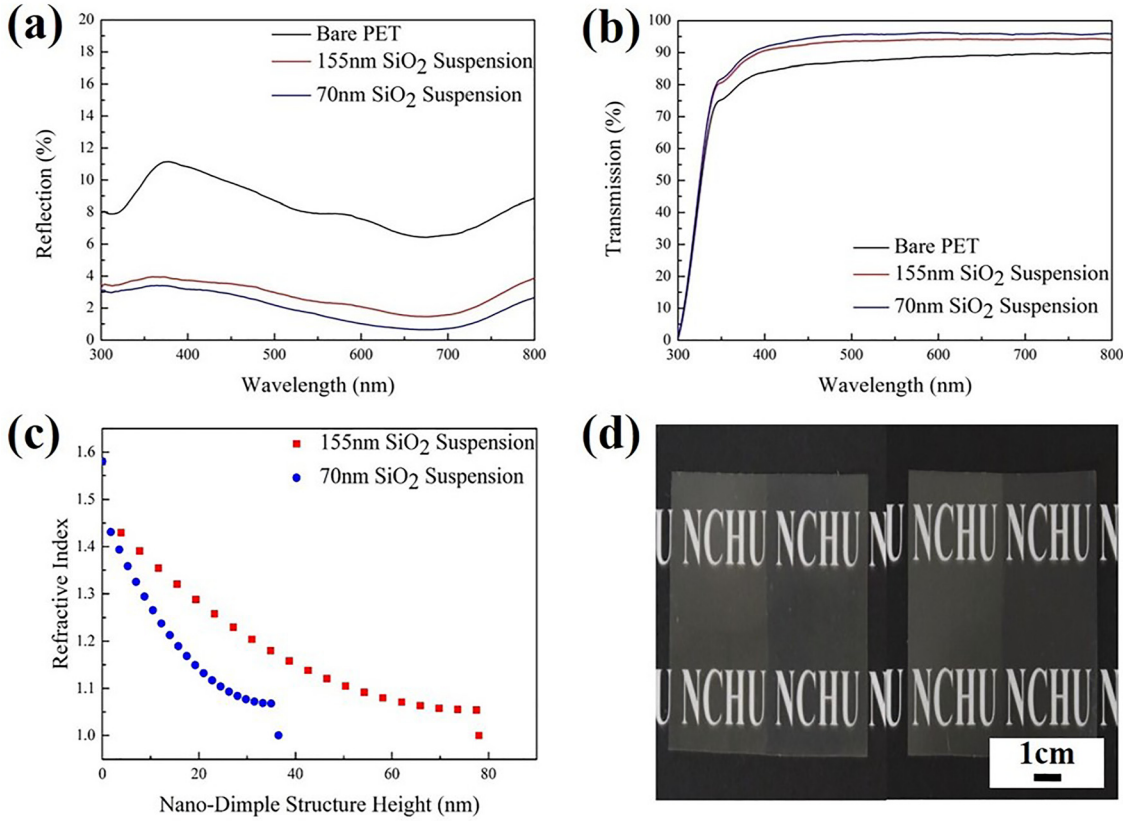

FIG. 3. (a) Normal incidence reflection spectra and (b) normal incidence transmission spectra obtained from a bare PET substrate and PET substrates coated with single-sided hemispherical nano-dimple arrays templated from 155 nm and 70 nm silica spheres, respectively. (c) Comparison of the change of calculated effective refractive index from the PET substrate (height = 0) to the top of the templated nano-dimple structure. (d) Photographs of PET substrates with the right halves coated with single-sided hemispherical nano-dimple arrays templated from 155 nm (left) and 70 nm silica spheres (right).

to 1.58, resulting in reduced reflectivity over visible light wavelength range. For hemispherical 155 nm nano-dimples (filled square), the change of effective refractive index is more moderate. Nevertheless, the reflectivity of that is a little higher than that of 70 nm nano-dimple coating. Owing to larger structure size and inter-structure distance, part of the incident light rays are reflected at the 155 nm nano-dimple structure surface, and part of the rays are refracted and then lost by absorption within the structures or emerge after several internal reflections. Hence, the incident light in the form of propagating energy is scattered off, indicating the 155 nm nano-dimple coating has slightly higher reflectivity and lower transmittance.

Figure 3(d) presents photographs of PET films with the right halves coated with single-sided hemispherical 155 nm nano-dimple arrays (left) and 70 nm nano-dimple arrays (right) illuminated with white light. The coatings are proven to be highly uniform, indicating that the intrinsic defects, as shown in Figure 2, do not considerably affect the optical uniformity of the coatings. Moreover, by comparing with the flat PET substrate, the significant reductions in optical reflection from the nano-dimple-structured coatings are observed. Importantly, it is evident that the 70 nm nano-dimple array-coated PET substrate shows higher transparency. The transparent coatings demonstrate that broadband antireflection coatings can be fabricated using the scalable Langmuir-Blodgett (LB) assembly approach. To assess the durability of the coatings, a pencil hardness test is applied to examine the mechanical properties of PET films coated with hemispherical 155 nm nano-dimple arrays. The pencil hardness of the coating is found to be 2H, indicating the hardness is good enough for normal use. In addition, the antireflection performance of the coating remains almost unchanged after abrasion test, only 1% reduction in the region of 400–900 nm is observed (Figure S1 in the supplementary material), showing an excellent abrasion-resistant property of this coating.

When the incident light encounters the surface of a substrate, an external reflection occurs. Subsequently, multiple internal reflections occur inside the substrate. This indicates that the transmittance of a PET substrate can be further increased not only by reducing the external reflection but also by suppressing the internal reflections. To experimentally confirm the above suggestions, monolayer hemispherical nano-dimple arrays are assembled directly on both sides of a PET substrate using the bottom-up assembly approach we developed. The photograph of a PET substrate with the right half coated with dual-sided hemispherical 155 nm nano-dimple arrays is displayed in Figure 4(a). The highly transparent sample reveals that the large domain scale hexagonal ordered nano-dimple structures are coated on both sides of the PET substrate (Figures 4(b) and 4(c)). In addition, compared to the single-sided nano-dimple-structured coating, as shown in Figure 3(d), the increased transparency further demonstrates that the internal reflections can be restrained by applying dual-sided nano-dimple-structured coatings. More importantly, the PET substrate coated with

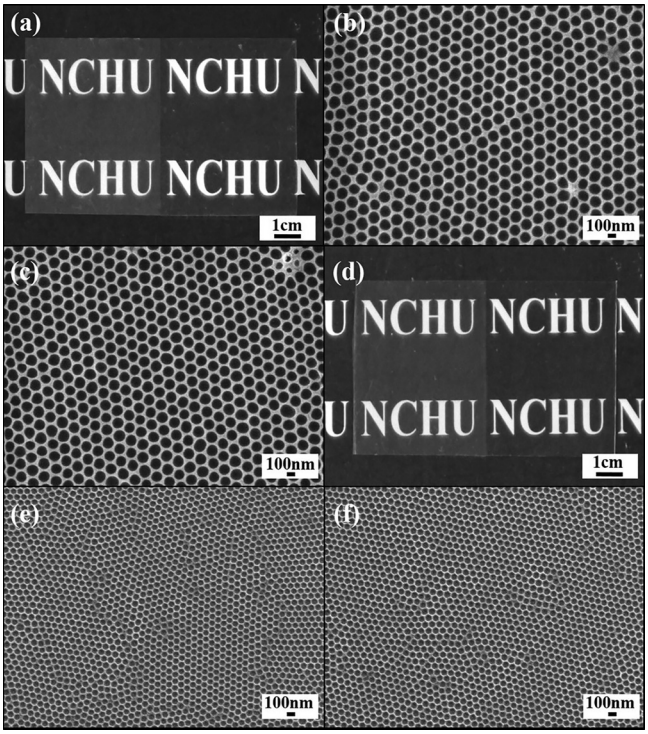

FIG. 4. (a) Photograph of a PET substrate with the right half coated with dual-sided hemispherical nano-dimple arrays templated from 155 nm silica spheres. (b) Top-view SEM image for the top side of the sample in (a). (c) Top-view SEM image for the bottom side of the sample in (a). (d) Photograph of a PET substrate with the right half coated with dual-sided hemispherical nano-dimple arrays templated from 70 nm silica spheres. (e) Top-view SEM image for the top side of the sample in (d). (f) Top-view SEM image for the bottom side of the sample in (d).

dual-sided 70 nm nano-dimple structures exhibits highest transparency (Figure 4(d)). This interprets that the long-range sub-100 nm nano-dimple-structured coatings on both sides of the PET substrate (Figures 4(e) and 4(f)) can further reduce the internal reflections.

Normal incidence reflection spectra obtained from the PET substrates coated with dual-sided hemispherical 155 nm and 70 nm nano-dimple arrays are presented in Figure 5(a), where measured reflectivities of the PET substrates coated with single-sided nano-dimple arrays are shown as references. It is observed that the reflectivity for the PET substrate with dual-sided 155 nm nano-dimple-structured coatings is less than 2%, while the PET substrate with dual-sided 70 nm nano-dimple-structured coatings yields a reflectivity of ~1% over visible light wavelength range. Compared to single-sided coatings, it is apparent that the broadband antireflection performance can be improved by implementing dual-sided coatings. In addition, owing to the higher refractive index of PET substrate than that of air, shorter grating period is capable to eliminate the higher-order diffractions in the internal reflections. As shown in Figure 5(b), the higher transmittance characteristics can be extended even to shorter wavelengths by introducing sub-100 nm period patterning. The PET substrate with dual-sided 155 nm nano-dimple-structured coatings shows an average transmittance of ~96%, while the transmittance is larger than 97% for the PET substrate with dual-sided 70 nm nano-dimple-structured coatings. Moreover, dual-sized coatings have higher transmittance at various incidence angles (Figures S2 and S3 in the supplementary material). The results can be interpreted by using Fresnel's equation

$$R = \left(\frac{n_1 - n_2}{n_1 + n_2}\right)^2$$

where R is the reflection at normal incidence from an interface between two materials with refractive index of n_1 and n_2. The theoretically calculated reflections of PET substrates with single-sided coatings are approximately equal to 5.3% (Figure 3(c)), majorly resulting from the internal reflection on the uncoated surface. In comparison with that, the calculated reflections of PET substrates with double-sided coatings are less than 0.5% (Figure S4 in the supplementary material). This indicates that dual-sized nano-dimple-structured coatings exhibit higher antireflection performance than single-sided coatings.

In conclusion, we have developed a scalable non-lithography-based self-assembly approach for simultaneously coating both sides of a PET substrate with periodic hemispherical nano-dimple structures. The optical measurements reveal that the resulting dual-sided sub-100 nm graftings exhibit improved broadband antireflection performance than single-sided coatings. Further structure optimization

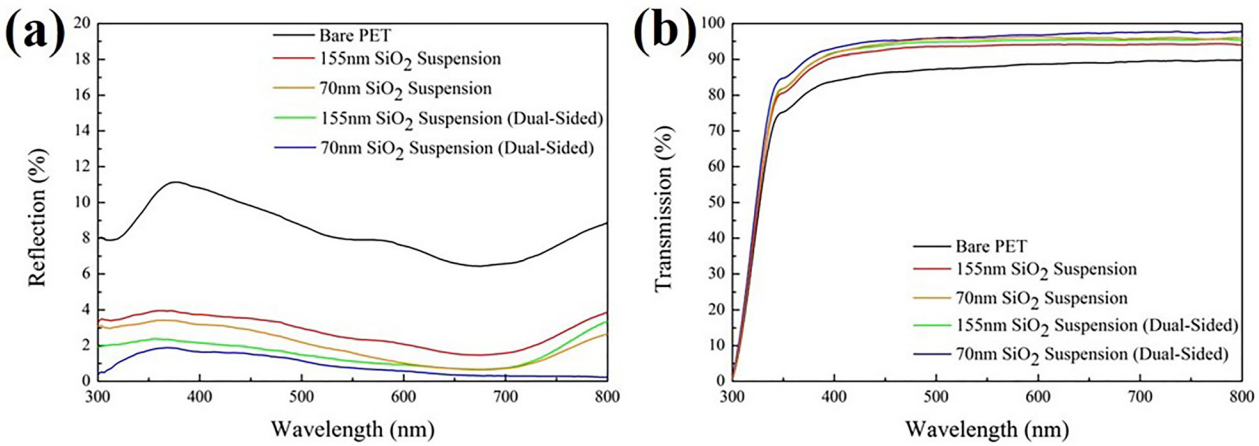

FIG. 5. (a) Normal incidence reflection spectra and (b) normal incidence transmission spectra obtained from a bare PET substrate and PET substrates coated with single-sided and dual-sided hemispherical nano-dimple arrays templated from 155 nm and 70 nm silica spheres, respectively.

and integration of nano-dimple-structured antireflection graftings in optical and optoelectronic devices are underway and will be reported in our future publications.

See supplementary material for the change in transmission of the coated PET substrate before and after abrasion, the optical transmission spectra of the coated PET substrate at various incidence angles, and the comparison of the change of calculated effective refractive index of the dual-sided nano-dimple structure.

Acknowledgment is made to National Science Council (Grant No. MOST 104-2221-E-005-086) for support of this research.

[1]I. Zada, W. Zhang, Y. Li, P. Sun, N. Cai, J. Gu, Q. Liu, H. Su, and D. Zhang, Appl. Phys. Lett. **109**, 153701 (2016).
[2]Y. Lai, F. Pan, C. Xu, H. Fuchs, and L. Chi, Adv. Mater. **25**, 1682 (2013).
[3]J. Xu and Z. G. Guo, J. Colloid Interface Sci. **406**, 1 (2013).
[4]B. Wang, W. X. Liang, Z. G. Guo, and W. M. Liu, Chem. Soc. Rev. **44**, 336 (2015).
[5]M. Sun, G. S. Watson, Y. Zheng, J. A. Watson, and A. Jiang, J. Exp. Biol. **212**, 3148 (2009).
[6]S. Yu, Z. Guo, and W. Liu, Chem. Commun. **51**, 1775 (2015).
[7]K. Biswas, S. Gangopadhyay, H.-C. Kim, and R. D. Miller, Thin Solid Films **514**, 350 (2006).
[8]H. A. Macleod, *Thin-Film Optical Filters*, 2nd ed. (McGraw-Hill, 1989).
[9]Y.-F. Huang, Y.-J. Jen, L.-C. Chen, K.-H. Chen, and S. Chattopadhyay, ACS Nano **9**, 301 (2015).
[10]C.-H. Sun, A. Gonzalez, N. C. Linn, P. Jiang, and B. Jiang, Appl. Phys. Lett. **92**, 051107 (2008).
[11]S. Chattopadhyay, L. C. Chen, and K. H. Chen, Crit. Rev. Solid State Mater. Sci. **31**, 15 (2006).
[12]J. Q. Xi, M. F. Schubert, J. K. Kim, E. F. Schubert, M. Chen, S. Y. Lin, W. Liu, and J. A. Smart, Nat. Photonics **1**, 176 (2007).
[13]K. Askar, B. M. Phillips, X. Dou, J. Lopez, C. Smith, B. Jiang, and P. Jiang, Opt. Lett. **37**, 4380 (2012).
[14]W.-L. Min, B. Jiang, and P. Jiang, Adv. Mater. **20**, 3914 (2008).
[15]H. K. Raut, S. S. Dinachali, Y. C. Loke, R. Ganesan, K. K. Ansahantwi, A. Gora, E. H. Khoo, V. A. Ganesh, M. S. M. Saifullah, and S. Ramakrishna, ACS Nano **9**, 1305 (2015).
[16]K.-C. Park, H. J. Choi, C.-H. Chang, R. E. Cohen, and G. H. McKinley, ACS Nano **6**, 3789 (2012).
[17]K. Askar, B. M. Phillips, Y. Fang, B. Choi, N. Gozubenli, P. Jiang, and B. Jiang, Colloids Surf., A **439**, 84 (2013).
[18]Y.-C. Chen, Z.-S. Huang, and H. Yang, ACS Appl. Mater. Interfaces **7**, 25495 (2015).
[19]Y. Fang, B.-M. Phillips, K. Askar, B. Chio, P. Jiang, and B. Jiang, J. Mater. Chem. C **1**, 6031 (2013).
[20]J. Hao, N. Lu, X. Hu, W. Wang, L. Gao, and L. Chi, Chem. Mater. **21**, 1802 (2009).
[21]S.-H. Kim, J. W. Shim, J.-M. Lim, S.-Y. Lee, and S.-M. Yang, New J. Phys. **11**, 075014 (2009).
[22]M. Schmudde, C. Grunewald, C. Goroncy, C. N. Noufele, B. Stein, T. Risse, and C. Graf, ACS Nano **10**, 3525 (2016).
[23]D. Lee, M. F. Rubner, and R. E. Cohen, Nano Lett. **6**, 2305 (2006).
[24]J. Zhu, Z. F. Yu, G. F. Burkhard, C. M. Hsu, S. T. Connor, Y. Q. Xu, Q. Wang, M. McGehee, S. H. Fan, and Y. Cui, Nano Lett. **9**, 279 (2009).
[25]M. Toma, G. Loget, and R. M. Corn, Nano Lett. **13**, 6164 (2013).
[26]M. K. Hedayati, S. Fari, C. Etrich, F. Faupel, C. Rockstuhi, and M. Elbahri, Nanoscale **6**, 6037 (2014).
[27]M. K. Hedayati and M. Elbahri, Materials **9**(6), 497 (2016).
[28]K. Nishioka, T. Sueto, and N. Saito, Appl. Surf. Sci. **255**, 9504 (2009).
[29]Y. M. Song, H. J. Choi, J. S. Yu, and Y. T. Lee, Opt. Express **18**, 13063 (2010).
[30]J. U. Cai and L. M. Qi, Mater. Horiz. **2**, 37 (2015).
[31]W. Stöber and A. Fink, J. Colloid Interface Sci. **26**, 62 (1968).
[32]A. S. Dimitrov and K. Nagayama, Langmuir **12**, 1303 (1996).